

N-Carbon-Doped Binary Nanophase of Metal Oxide/Metal–Organic Framework for Extremely Sensitive and Selective Gas Response

Hyegi Min, Ohchan Kwon, Jihyun Lee, Eunji Choi, Jihee Kim, Nahyeon Lee, Kiwon Eum, Kyu Hyoung Lee, Dae Woo Kim,* and Wooyoung Lee*

Metal–organic frameworks (MOFs), which are highly ordered structures exhibiting sub-nanometer porosity, possess significant potential for diverse gas applications. However, their inherent insulative properties limit their utility in electrochemical gas sensing. This investigation successfully modifies the electrical conductivity of zeolitic imidazole framework-8 (ZIF-8) employing a straightforward surface oxidation methodology. A ZIF-8 polycrystalline layer is applied on a wafer-scale oxide substrate and subjects to thermal annealing at 300 °C under ambient air conditions, resulting in nanoscale oxide layers while preserving the fundamental properties of the ZIF-8. Subsequent exposure to NO₂ instigates the evolution of an electrically interconnected structure with the formation of electron-rich dopants derived from the decomposition of nitrogen-rich organic linkers. The N-carbon-hybridized ZnO/ZIF-8 device demonstrates remarkable sensitivity ($\approx 130 \text{ ppm}^{-1}$) and extreme selectivity in NO₂ gas detection with a lower detection limit of 0.63 ppb under 150 °C operating temperature, surpassing the performance of existing sensing materials. The exceptional performances result from the Debye length scale dimensionality of ZnO and the high affinity of ZIF-8 to NO₂. The methodology for manipulating MOF conductivity through surface oxidation holds the potential to accelerate the development of MOF-hybridized conductive channels for a variety of electrical applications.

1. Introduction

Metal–organic frameworks (MOFs) are a class of highly versatile materials, acclaimed for their immense potential in gas-related applications owing to their expansive porous structure and precisely defined crystallographic configuration.^[1] The well-ordered porous structure allows for molecular sieving, facilitating the filtration of specific molecules, whilst their atomic scale features significantly enhance the interaction between the gas and the framework. These characteristics have accelerated the application of MOFs across various domains, including gas separation,^[2–6] storage,^[7–9] and catalysis.^[10–13] Nevertheless, the successful implementation of these high-throughput properties in gas analysis does not straightforwardly translate to their usage in electrochemical gas sensing devices. A primary obstacle arises from the electrically insulating properties of MOFs. Alternatives could be the hybridization of MOF layers onto conductive sensing

H. Min, J. Lee, J. Kim, K. H. Lee, W. Lee
Department of Materials Science and Engineering
Yonsei University
50 Yonsei-ro, Seodaemun-gu, Seoul 03722, Republic of Korea
E-mail: wooyoung@yonsei.ac.kr

H. Min
KIURI Institute
Yonsei University
50 Yonsei-ro, Seodaemun-gu, Seoul 03722, Republic of Korea

H. Min
Nick J. Holonyak Micro and Nanotechnology Laboratory
University of Illinois at Urbana–Champaign
Urbana, IL 61801, USA

O. Kwon, E. Choi, D. W. Kim
Department of Chemical and Biomolecular Engineering
Yonsei University
Yonsei-ro 50, Seodaemun-gu, Seoul 03722, Republic of Korea
E-mail: audw1105@yonsei.ac.kr

O. Kwon
Department of Chemistry
University of California
Berkeley, Berkeley, CA 94720, USA

N. Lee, K. Eum
School of Chemical Engineering
Soongsil University
Seoul 06978, Republic of Korea

 The ORCID identification number(s) for the author(s) of this article can be found under <https://doi.org/10.1002/adma.202309041>

DOI: 10.1002/adma.202309041

materials, such as metal oxides, graphene derivatives, or MXenes.^[14–19] This approach seeks to leverage the molecular sieving mechanism of MOFs to eliminate the influence of unwanted species.^[20] However, challenges still exist, with unstable anchoring, inadequate coverage, and constrained operating conditions posing significant hindrances. Furthermore, the intrinsic sensing properties remain substantially influenced by the properties of the conducting channel. Recently, several studies have reported MOF-derived oxide sensors through thermal oxidation reactions. These resulting oxides exhibit a conductivity range suitable for electrochemical sensing.^[21–23] While these sensors are often distinguished from conventional oxide sensors, a key question remains unanswered whether these sensing materials retain the outstanding gas analysis properties inherent to MOF structures, even after thermal annealing.

In response to the imperative for the development of conducting MOFs, contemporary research has pivoted toward the synthesis of MOFs with adjustable conductivity. This is achieved by manipulating the functional organic linkers and metal centers to promote the conjugation of adjacent orbitals.^[21] For instance, MOFs constructed from relatively softer and electropositive organic ligands, such as nitrogen and sulfur, are reported to enhance the covalency between the metal center and linker.^[22–24] Further, the integration of ligands bearing chelating groups is known to augment the conjugation between the metal and ligand, thereby facilitating enhanced electron delocalization.^[25–29] In addition, the assembly of planar organic ligands induces π - π stacking of the organic components, consequently creating conductive pathways amidst the organic layers.^[30–33] By utilizing these strategies, many studies have successfully demonstrated the functionality of chemiresistive gas sensors for the detection of a wide spectrum of gaseous compounds, including volatile organic compounds (VOCs) and hydrocarbons.^[25,34,35] Nevertheless, despite exceptional detection abilities, these conducting MOF-based chemiresistors include limitations like slow response times, irreversible reactions, and low detection selectivity. Additionally, the feasibility of large-scale device production, along with the chemical stability of conducting MOFs in extreme oxidation/reduction conditions, requires further assessment to broaden their application scope. Thus, the advancement of electrically conductive MOF materials that exhibit superior sensitivity and selectivity for detection, in conjunction with the enablement of large-scale fabrication, is critical for the development of high-performing electrochemical sensors.

Herein, we introduce a new concept of a conducting channel, hybridized with a binary architecture of ZnO/zeolitic imidazole framework (ZIF)-8 crystals, further amalgamated with nitrogen-doped carbon compounds (termed N-Carbon-ZnO/ZIF-8, or CZZ). Remarkably, this nanochannel exhibits exceedingly high selectivity and responsivity toward NO₂, even in the presence of water, in diverse gas mixtures under operating conditions of 150 °C. This outstanding performance is achieved via a straightforward fabrication process involving the control of surface oxidation of ZIF-8 in air, followed by exposure to NO₂. Gas-sensing performance of the sensor surpasses previous gas sensor materials including metal oxides, 2D materials, porous carbons, and covalent organic frameworks, among others. Importantly, the starting ZIF-8 layer can be coated onto a large substrate equipped with pre-patterned electrodes, rendering this gas sensor fabrication

procedure highly scalable. Additionally, we investigated the variations in the surface structure of ZIF-8 induced by different oxidation conditions and their subsequent effects on gas adsorption and response properties. This analysis helps shed light on the gas interaction mechanism within the hybridized structure. Our approach not only facilitates large-scale fabrication but also offers a new perspective on the application of MOF materials in electronic devices necessitating gas-selective conducting channels.

2. Results and Discussion

2.1. Fabrication and the Morphological Characterization of the CZZ Device

Figure 1a presents a sequential graphical depiction of the fabrication processes, with accompanying scanning electron microscopy (SEM) images corresponding to each phase (Figure 1b–d). Initially, SiO₂ substrates were employed, and interdigitated electrodes, each with a width of 20 μ m and comprised of 5 μ m of Au, were patterned onto them to ensure optimal contact between the electrodes and the MOF layers (Figure S1, Supporting Information). It is noteworthy that conventional post-deposition methodologies, such as spray coating, are unsuitable for realizing reliable device fabrication due to the coarse surfaces of MOF crystals, which obstruct uniform contact with the electrodes. To overcome this challenge, the substrate equipped with patterned electrodes was immersed in an aqueous solution containing ZIF-8 precursors, specifically 2-methylimidazole (2-MeIM) and Zn ions, and a subsequent hydrothermal growth process was conducted at 50 °C.^[36,37] The interplay between the ZIF-8 precursors, silicon oxide surface, and the Au electrodes promotes ZIF-8 nucleation and results in the formation of dense polycrystalline layers after \approx 1 h (as seen in Figure 1b). ZIF-8 was selected among the MOFs due to its wide adoption, ease of forming continuous films, and its ability to oxidize into ZnO, a material extensively utilized in gas sensing applications. These attributes render ZIF-8 among the most fitting MOFs for developing responsive gas-sensing devices.^[38–40] Figure 1e shows the wafer with the electrode array after ZIF-8 growth. We emphasize that the simple fabrication process facilitates the production of multiple devices on a wafer scale, thereby boosting scalability and production yield.

The ZIF-8 layer is subjected to thermal annealing at an optimized temperature of 300 °C in air conditions. This process fulfills dual roles: initiating selective oxidation of the ZIF-8 surface and preserving the ZIF-8 structure within the inner particles. There is much literature reporting the carbonization of MOFs in inert gas and at higher temperatures to avoid oxidation and obtain a high carbon yield.^[41] However, thermal treatment at a mild temperature in the presence of oxygen is critical in our study to generate a semiconducting oxide channel while preserving the MOF structure. Figure 1c presents an SEM image that demonstrates the consequences of thermal annealing, revealing the formation of cracks at domain boundaries and enhanced porosity on crystal surfaces while the ZIF-8 layer is still observed. As observed during the decomposition of polycrystalline materials, the ZIF-8 layer displays lower stability at the grain boundaries.^[42] This instability may be attributed to various factors, such as structural rearrangements, phase separation, or elevated surface

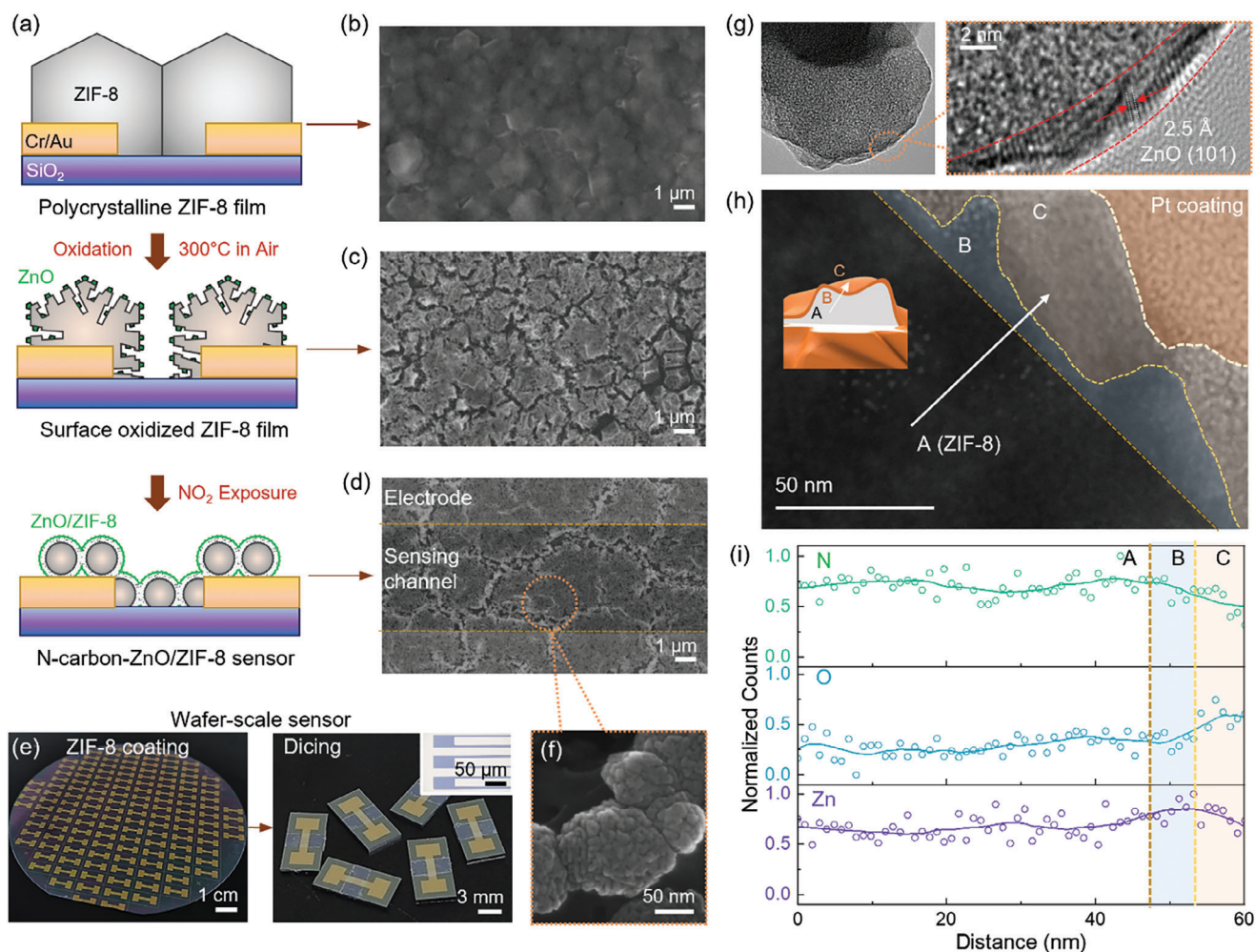


Figure 1. Photographic and electron microscope images of the prepared gas sensors and their sensing channel. a) Graphical illustration and b–d) SEM images depicting the fabrication procedure of the N-carbon doped ZnO/ZIF-8-based NO₂ sensors. e) Photographic image depicting the ZIF-8 coated electrodes. f) High-magnification SEM image of the ZnO/ZIF-8 morphology after NO₂ exposure. g) TEM images of ZIF-8 particle oxidized at 300 °C in air. h) Cross-sectional STEM image of the thermally annealed ZIF-8 coating at 300 °C followed by NO₂ exposure. Graphical illustration of the cross-section is depicted in the inset for clarity. Note that the C section is the projection of the surface seen from the viewing axis. i) Elemental composition line scanning data obtained from the regions marked with a white arrow.

energies. These phenomena induce localized structural alterations and the emergence of cracks, thereby increasing porosity and surface roughness in the annealed ZIF-8 layer. Alongside decomposition, surface Zn species are transformed to form nanometer-scale ZnO clusters, depicted as green dots in Figure 1a. Subsequent exposure to NO₂ prompts the thermally annealed ZIF-8 layer to develop an interconnected morphology, rendering individual grains undetectable at low magnification (Figure 1d). The magnified SEM image reveals the presence of interlinked particles that exhibit a unique surface morphology with many creases and ridges (Figure 1f). During the NO₂ treatment, the surface ZnO clusters merge to form interconnected electron-conducting channels bolstered by the intervening ZIF-8 layers. The remaining carbon species from the decomposed 2-MeIM are also hybridized with the ZnO/ZIF-8 structure.

To explore the surface morphology of the ZIF-8 particles further, we utilized transmission electron microscopy (TEM) and

scanning transmission electron microscopy (STEM) with energy-dispersive X-ray spectroscopy (EDS) following each preparation procedure. Upon thermal treatment at 300 °C (before NO₂ exposure), the particle surfaces displayed ≈2 nm thick lattice structures corresponding to the (101) plane of ZnO, with a d-spacing of 2.5 Å (Figure 1g) (ICDD # 36–1451). This crystalline lattice was absent in the inner particles, indicating that ZnO formation was restricted to the ZIF-8 crystal surface. Moreover, STEM-EDS analysis disclosed heightened counts of O and Zn species localized at the crystal's outer edges, corroborating the presence of a ZnO layer a few nanometers thick (Figure S2, Supporting Information).

Figure 1h portrays the cross-sectional STEM image of the particles after NO₂ exposure, obtained via focused ion beam cutting. These sections are split into three portions labeled A, B, and C. Figure 1i provides the elemental line scanning data, which was acquired at the regions denoted with a white arrow and tra-

verses all three sections. It should be noted that section C is not the cross-section of the particle but a surface projection at the viewing angle resulting from the creased morphology, as illustrated in the graphical inset. The relatively stable elemental analysis suggests that section A primarily comprises a homogeneous phase ascribed to the underlying ZIF-8, which is shielded by the surface oxide layer during NO₂ exposure. Section B exhibits a mild increase in O species, in conjunction with the presence of Zn and N species, indicating a hybridized state of organic phases and ZnO within the layer. Section C shows a further increase in O content while N and Zn species decrease, suggesting a distinct environment localized at the particle surface. The characterization of surface properties will be further clarified in the ensuing sections, employing X-ray photoelectron spectroscopy (XPS) depth profiling results. Nonetheless, these observations confirm that the hybrid channel is formed on the ZIF-8 surface, where its dimension is confined by several nanometer scales.

2.2. Effects of Thermal Annealing Temperature on the Morphology of ZIF-8

To understand the effects of the thermal annealing process, polycrystalline ZIF-8 films on SiO₂ substrates and ZIF-8 single crystal powders were separately prepared and subjected to varying temperatures (200, 300, 400, and 500 °C) under an air atmosphere for an hour. SEM and contact angle measurements were acquired by the ZIF-8 films, which were interpreted for the morphological change of the ZIF-8 films focusing on the changes in grain boundary properties. Other characterization tools such as X-ray diffraction (XRD), Fourier-transform infrared spectroscopy (FT-IR), Raman, and N₂ gas adsorption isotherms were tested with ZIF-8 crystal powder, which was investigated to emphasize the change in intrinsic structural properties of the MOF phase upon thermal annealing.

Figure 2a presents SEM images, in conjunction with contact angle measurements, of thermally treated ZIF-8 films. The SEM image analysis implies a proportional relationship between the prevalence of crystal boundary fissures and the temperature increase. In-depth observation at an amplified magnification suggests that the morphology of the individual crystals remains unaltered up to a thermal threshold of 200 °C. However, when the ZIF-8 films are subjected to a temperature of 300 °C, nanopores become visible, with dimensions varying between 10 and 100 nm, on the surface of the crystal. Further increase in temperature to 400 °C results in a decreased surface porosity due to the development of more substantial ZnO layers, as depicted in Figure S3 (Supporting Information). It has been noted that polycrystalline films undergo remarkable morphological transformations at a comparably modest temperature of 200 °C, while the structure of single-crystal particles remains relatively unaffected. Previous research suggested that for polycrystalline MOF films grown on a substrate, strain at the substrate-MOF layer interface fosters structural collapse,^[43] consistent with our observations. Further, contact angle measurements indicate an overall trend of decreasing hydrophobicity with increasing annealing temperature. Intriguingly, a marked decrease in the hydrophobicity of the surface is observed within the temperature range of 300–400 °C, which

can be due to the generation of hydrophilic ZnO layers, as we observed in the TEM analysis (Figure 1g,h).

Figure 2b displays XRD patterns, which suggest the persistence of the ZIF-8 crystal phase up until a temperature of 300 °C. Notably, the ZIF-8 phase becomes undetectable, and the emergence of ZnO-associated peaks is observed when the temperature increases above 400 °C. This observation aligns with the manifestation of surface oxidation detected in the SEM images. Complementary to these observations, FT-IR spectra presented in Figure S4a (Supporting Information) corroborate the presence of similar chemical bonds in the ZIF-8 films processed at temperatures below 400 °C. On the contrary, samples subjected to heat treatment at 400 and 500 °C display diminished intensities of characteristic ZIF-8 peaks while revealing emergent Zn–O peaks at 500 cm⁻¹. We like to mention that even when subjected to temperatures exceeding 400 °C, where substantial carbon oxidation is expected, peaks corresponding to carbon bonds, such as the C=C and C–H bonds at 1650 and 2960 cm⁻¹, continue to appear. This observation implies the presence of organic residues within the ZnO phase, as the applied temperature is insufficient to entirely decompose carbon species, and the exposure time is constrained to a 1-hour duration. N₂ isotherm results also imply a distinct transition between the 300–400 °C, where only the ZIF-8 annealed below 400 °C shows a substantial increase of adsorption quantity in the lower pressure regions attributed to microporous materials (Figure 2c). Consequently, the calculated Brunauer–Emmett–Teller (BET) surface area decreases from 1238 to 46 cm² g⁻¹ at the transition temperature of 300–400 °C. Pore size distribution reveals that the thermal treatment facilitates the formation of meso/macropores spanning 20–40 nm (Figure 2d), which is consistent with the SEM results (Figure 2a).

Figure S5 (Supporting Information) provides evidence for the simultaneous existence of multiple phases in the samples subjected to thermal treatment beyond 300 °C, as inferred from the observed color variation and the associated reflectance spectra. As illustrated in Figure S5a (Supporting Information), the initial pale yellow tint of the white ZIF-8 gradually turns into brown and pink shades upon exposure to temperatures increasing from 300 °C. Concurrently, the reflectance properties of the ZIF-8 gradually transition to the characteristic of ZnO, and the alteration is particularly visible in the sample treated at 300 °C (Figure S5b, Supporting Information). This shift in the reflectance spectra indicates the formation of ZnO and the structural transformation of the material. Moreover, the Tauc-plot portrays a reduction in band-gap energy corresponding to increasing temperature (Figure S5c, Supporting Information). A noteworthy reduction in band-gap energy, to the value of 2.42 eV, is observed within the temperature range of 300–400 °C, supporting ZnO formation. Similarly, despite a relatively consistent work function, the dramatic fall in the Fermi level underscores a phase transition toward ZnO (Figure S5d,e, Supporting Information). It is crucial to highlight that the unusual colors observed in the ZnO samples prepared at 400 and 500 °C, coupled with their comparatively lower band-gap energy (2.67 and 2.15 eV versus ≈3.37 eV for bulk ZnO), suggest that the ZnO is electrically doped with hybridized organic residues.^[44,45] Considering the electron microscopy results in conjunction with the presented XRD, FT-IR, Raman spectra, N₂ adsorption isotherm analysis, and light absorption properties, the acquired data collectively indicate a sharp

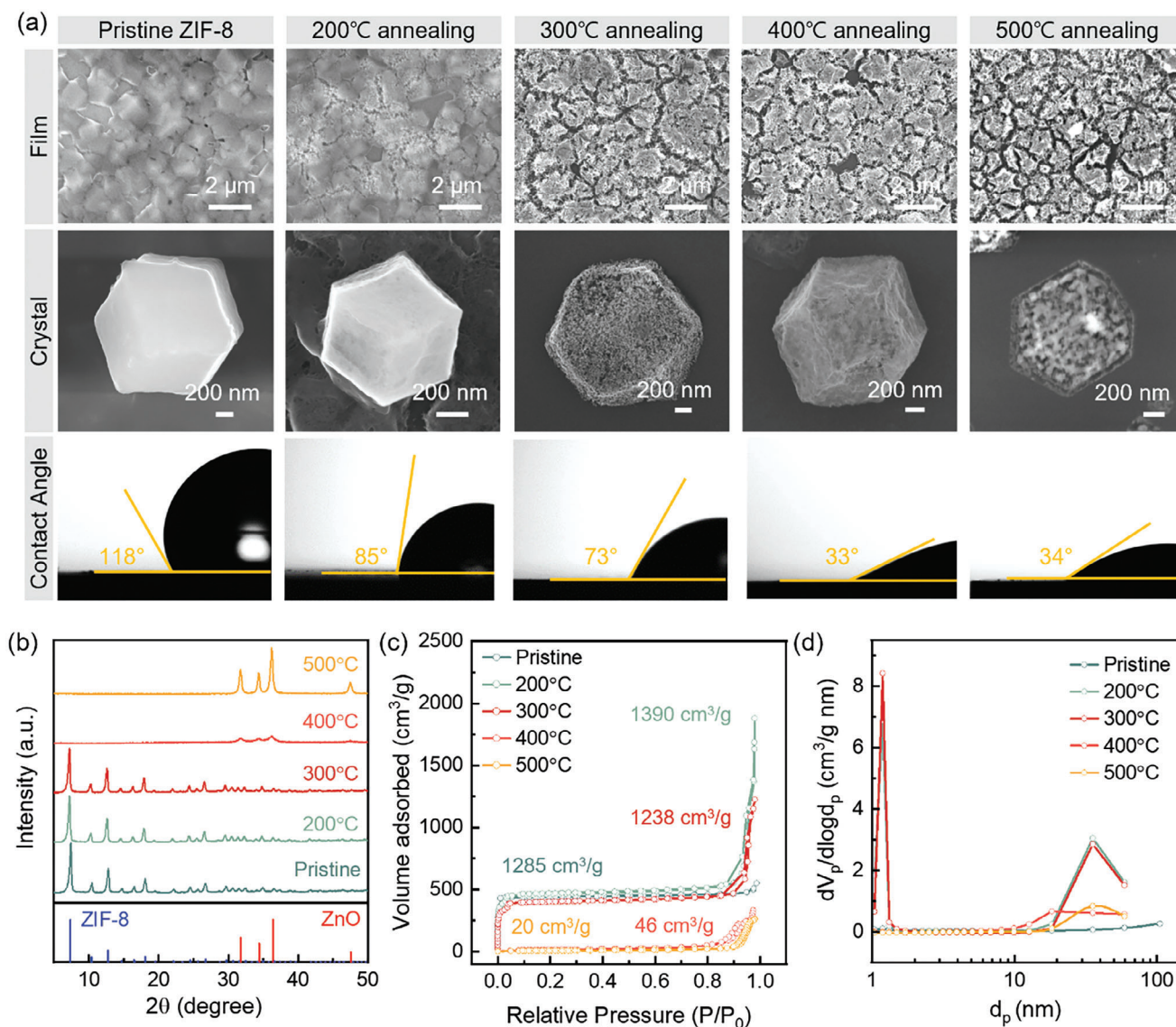


Figure 2. Influence of temperature on the evolution of ZnO/ZIF-8 structure. a) Low and high magnification SEM images of the ZIF-8 coatings and particles after annealing at different temperature and their corresponding water contact angle data. b) XRD patterns, c) N₂ adsorption isotherms measured at 77 K, and their corresponding d) pore size distribution data of thermally annealed ZIF-8 particles.

phase transition of ZIF-8 to ZnO between 300–400 °C. We further highlight that to form conductive channels with nanometer-level thickness upon NO₂ exposure, nanometer-sized ZnO clusters are required to exist locally on the surface of ZIF-8. 300 °C was found to be the critical oxidation temperature for the formation of these structures.

2.3. The Localized Surface and Depth Chemical Structure of CZZ-300 Nanochannel

We found that thermal treatment plays a critical role in forming ZnO nanochannels, but it can also induce organic linker decomposition into carbon residue at the same time. In addition, the subsequent exposure to NO₂ is primarily expected to affect

the organic species originating from the ZIF-8 ligands. This is due to the strong oxidative nature of NO₂, which is well-known to degrade ZIF-8, while the relatively high stability of the inorganic ZnO phase will maintain its structure and properties.^[46] To verify our assumption on the effect of thermal annealing and NO₂ exposure on the chemical structure of ZIF-8, XPS depth scanning techniques were utilized on ZIF-8 films grown on SiO₂ substrates. Additionally, we carried out ¹³C and ¹⁵N solid-state nuclear magnetic resonance spectroscopy (SS-NMR) techniques, specifically with ZIF-8 single-crystal powders. For brevity reasons, we will label the thermally treated ZIF-8 at 300 °C as CZZ-300 where further exposure to NO₂ will be signified as CZZ-300 + NO₂.

First, XPS depth scanning was employed to further investigate the chemical composition and bonding within different

depths of the device (Figure 3a,b; Figure S6, Supporting Information). Figure 3a displays the deconvoluted elemental spectra of the Zn2p_{3/2}, N1s, C1s, and O1s regions. The bottom two rows depict the surface XPS spectra of pristine ZIF-8 and the thermal-treated CZZ-300, respectively. The third row shows spectra obtained from the surface of the NO₂-exposed sample, CZZ-300 + NO₂, while the top two depict the spectra acquired in 0.5 nm depth intervals. In the Zn2p_{3/2} spectra, three major peaks at 1022.5, 1021.5, and 1020.8 eV were observed and assigned to Zn–O, Zn–N, and Zn–C bonds, respectively.^[47,48] The appearance of the Zn–O bond from CZZ-300 indicates surface oxidation resulting from the thermal treatment of the ZIF-8. Upon NO₂ exposure (CZZ-300 + NO₂), the overall peak shifted to lower energies by ≈0.7 eV, suggesting the formation of more electron-rich environments.^[49] This shift is primarily attributed to the evolution of the Zn–C peak and the reduction of the Zn–N peak. At a depth below 0.5 nm, the peak shift returns to a similar state to the CZZ-300 sample. The N1s spectra were deconvoluted into three peaks. 400.3 and 398.2 eV peaks were assigned to pyrrolic and pyridinic N, respectively, originating from the N sites in the 2-MeIM ligands.^[50] The peak at 399.2 eV was attributed to N–Zn bonds. The presence of the two ligand peaks in the surface spectra suggests the presence of surface defects in the ZIF-8 with unbound imidazole sites. Interestingly, the most significant variation in peak structure was observed on the surface of the CZZ-300 + NO₂, with prominent peak splitting attributed to a decrease in the N–Zn peak. In contrast, the underlying phase retained a high N–Zn ratio, indicating the presence of unaffected ZIF-8 layers.

The C1s spectra were deconvoluted into four peaks, assigned to C=O, C–O (or C–N), C–C, and C–Zn bonds located at 288.3, 285.7, 284.4, and 283.5 eV, respectively.^[51,52] The C=O and C–O bonds indicate the presence of exterior carbonate group terminations, which can also arise from surface defects consistent with the N1s analysis.^[53] Examination of the C1s spectra also reveals a distinct environment on the surface of the CZZ-300 + NO₂, with a down-shifted peak, suggesting the formation of electron-rich chemical states associated with the C–Zn bond. This peak shift is again not observed, and a single peak is observed in the underlying layers, which can be attributed to the C species in the imidazolate ligands of the remaining ZIF-8. The O1s spectra were analyzed employing three peaks at 532.5, 531.9, and 530.9 eV, identified as O_{Ads}, O_{Def}, and O_{Lat}, respectively. The O_{Ads} peak corresponds to O species adsorbed on the ZIF-8 surface, such as water molecules.^[53,54] The O_{Def} peak can arise from Zn–OH groups on ZIF-8 surfaces or dissociated O located at vacancies from the ZnO layer (O^I), and the O_{Lat} peak is associated with the lattice oxygens of the oxide (O^{II}).^[54] The observed shift of the O1s peak to lower binding energy for the CZZ-300 is attributed to the formation lattice oxygens from the ZnO lattice. This shift becomes more pronounced after NO₂ exposure (CZZ-300 + NO₂), indicating the oxidative nature of NO₂ and its contribution to the thickening of the oxide layer.

The elemental composition analysis presented in Figure 3b confirms the higher concentration of C and O species on the surface of the CZZ-300. This finding aligns with the spectra deconvolution analysis in Figure 3a, which identified the presence of Zn–C bonds and the formation of oxide species after NO₂ exposure. We note that the XPS spectra for the CZZ-300 + NO₂ ob-

tained at a depth below 1 nm show no significant peak shifts, indicating the existence of a homogeneous phase without any modification (Figure S6, Supporting Information). The XRD spectra in Figure S7 (Supporting Information) also reveal that the ZIF-8 phase is present even after NO₂ exposure. The relatively higher peak intensity after the NO₂ exposure in the thermally annealed sample indicates that the formed ZnO aids in the protection of the underlying ZIF-8 phase by forming a barrier layer.

The nature of chemical bonding of the organic phase following NO₂ exposure was further explored by employing ¹³C and ¹⁵N SS-NMR techniques (Figure 3c,d). It is important to highlight the hybridized composition of these materials, which introduces complexity in defining the precise chemical structures for the CZZ-300 + NO₂ sample. Nonetheless, discernable alterations in the spectra provide key insights into the chemical variations corresponding to each treatment step, especially regarding the effect of NO₂ exposure. Each C and N atom is designated in Figure 3e,f, demonstrating the suggested reaction pathway between NO₂ and ZIF-8.^[55–57] The SS-NMR signal for the 2-MeIM linker is provided as a reference, illustrating distinct peaks for all C and N species. While we cannot exclude the possibility of reaction or interaction between NO₂ and residual carbons developed from the initial thermal annealing step, we focused on the reaction between the dominating phase of ZIF-8, where oxidation mainly occurs on the particle surface.

Compared to the pristine 2-MeIM signal, the deprotonation and bonding of nitrogen groups to zinc ions impose symmetry onto the ZIF-8 molecule, leading to the unification of the discrete C⁴–C⁵ and N¹–N³ signals. The merged peaks of the ZIF-8 phase appear with doubled intensity at 124 and 205 ppm in the ¹³C and ¹⁵N SS-NMR spectra, respectively. In line with the FT-IR findings (Figure S4a, Supporting Information), the chemical bonding states of the pristine and thermally annealed ZIF-8 (CZZ-300) reveal no significant differences, suggesting that the primary phase predominantly comprises ZIF-8 even after thermal oxidation. Upon exposure to NO₂, the ¹³C NMR spectra present additional shoulder peaks at 147 and 126 ppm (Figure 3c), corresponding to the C^{2*} and C^{4*} signals (Figure 3f), respectively. Furthermore, a broad peak emerges at 118 ppm, designated as C^{5*}, indicating NO₂ substitution on the C⁴ carbons, thereby disrupting the symmetry of the molecule. Comparing these peaks with the C⁴ and C⁵ peaks of 2-MeIM reveals that the C^{4*} and C^{5*} peaks are located 2–3 ppm downfield. This downfield shift is attributed to the highly electrophilic nature of the NO₂ groups, leading to the deshielding of the carbon atoms.^[58] The ¹⁵N spectra, on the other hand, discernably exhibit only a single peak at 170 ppm denoted with a *, likely due to the high signal-to-noise ratio, which complicates the resolution of multiple peaks for nitrogen atoms in the sample (Figure 3d). Nonetheless, the signal position resembles the hydrogen-terminated N^{1'} of the 2-MeIM linker, potentially signifying the cleavage of Zn–N bonds (Figure 3d). The observation is consistent with the XPS N1s results and previously reported degradation pathways under oxidative conditions.^[46,59]

Drawing upon the aforementioned characterizations, Figure 3g outlines the transformation pathway of the ZIF-8 derivatives through thermal oxidation and NO₂ exposure and depicts the hybridized structure of the CZZ channel. Initially, ZIF-8 polycrystalline films are generated via a hydrothermal process. Upon undergoing thermal treatment at 300 °C, the film

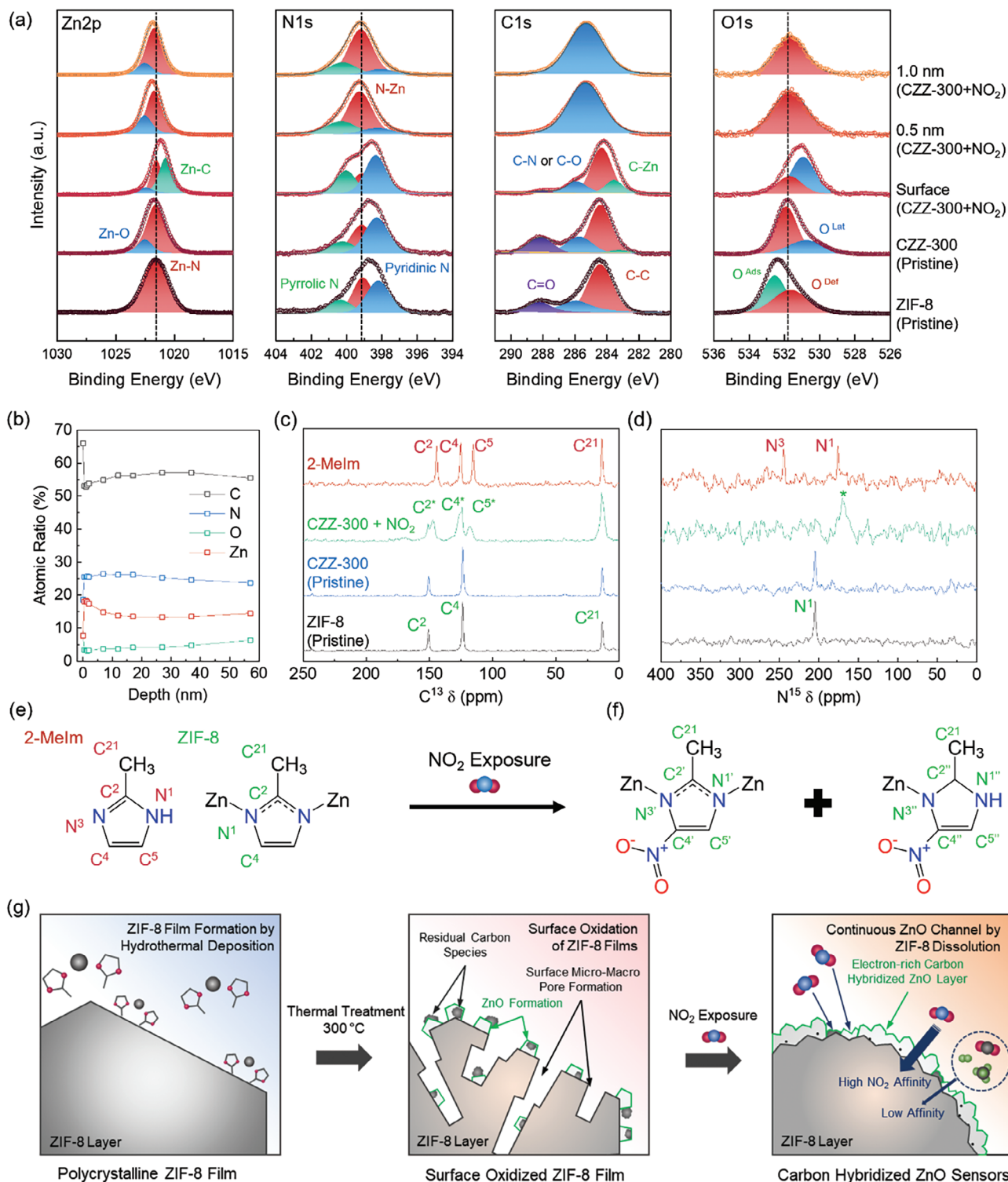


Figure 3. Chemical structure of ZIF-8 after thermal oxidation and NO₂ exposure. a) Detailed XPS peak spectra of Zn2p, N1s, C1s, and O1s from the depth-resolved survey of the NO₂ exposed sensors and b) its atomic composition data. For the experiment, NO₂-exposed ZIF-8 (300) film sensors were etched by Ar ion. c) ¹³C, d) ¹⁵N solid-state NMR data of pristine ZIF-8, ZIF-8 (300), and after NO₂ exposure. e) Molecular structure notation for the corresponding peaks from the NMR data. f) Possible residues of ZIF-8 upon NO₂ exposure. The C^{2*}, C^{4*}, C^{5*} peaks are possibly a combination of C² + C^{2'} + C^{2''}, C⁴ + C^{4'} + C^{4''}, C⁵ + C^{5'} + C^{5''}. g) Illustration depicting the transformation of the ZIF-8 sensors during the fabrication process.

primarily comprises porous, defective ZIF-8 structures hosting localized ZnO clusters. These clusters are predominantly located on the external surface of the ZIF-8 particle and are tarnished with carbon residues from the organic linkers. Significantly, when NO₂ is introduced, the ZnO layer consolidates into thin, continuous nanochannels upon dissolution of the ZIF-8 phase. Furthermore, the residual carbons and remaining organic linkers from the ZIF-8 phase undergo additional hybridization with the oxides. The SS-NMR results indicate the appending of electrophilic NO₂ on the 2-MeIm linker facilitates the cleavage of the Zn–N bonds in ZIF-8. As seen from the XPS results, these open coordinate Zn sites may recouple with the organic residues enabling doping of the surface ZnO. Considering the TEM observation in Figure 1b and the XPS depth profile study, this hybridized layer is expected to be extremely thin in several nanometer scales. This process facilitates the simultaneous formation of nanometer-thick, continuous ZnO layers with a dimension scale comparable to the Debye length, along with the hybridization of N- and C-based organic species.

2.4. Gas Detection Properties of the CZZ Device

In previous studies, various bulk types of ZIF-8 and ZnO have been widely used for selective medium or gas detection.^[18,38,60] To find feasible applications of CZZ devices, we investigated the gas detection properties by fabricating chemiresistor. We selected NO₂ as the target gas due to its high reactivity, which permits us to assess the stability of both the sensing channel and the inner ZIF-8 core under robust oxidizing conditions.^[46] Because the ZnO phase functions as the gas reaction place, we explored the optimal operating temperature for the sensing layer. This was achieved by exposing the device to 10 ppm NO₂ gas at a variety of temperatures (Figure 4a). In the presence of NO₂ gas, a sharp increase in resistance value was observed, signifying an electron exchange reaction between the n-type ZnO and the highly electrophilic NO₂ molecules.^[61] A response was measurable from 100 °C, but the desorption of NO₂ molecules was substantially slower as compared to those at higher temperatures. The signal amplitude was the highest at 150 °C, which then showed a gradual reduction along with temperature increment. From the resistance curve obtained (Figure S8, Supporting Information), we observed a sequential decrease in the baseline resistance corresponding to an increase in operating temperature. This pattern aligns with the characteristics of semiconducting materials, wherein the conductance increases at higher temperatures owing to the increased number of thermally-excited electrons in the band structure. Therefore, it seems that proper resistance range is achieved at the temperature range ≈150 °C.

We further investigated the impact of thermal oxidation conditions and measurement temperature on gas detection properties (Figure 4b; Figure S9, Supporting Information). It is understood that the density of oxide and crystallinity are highly influenced by the annealing temperature (Figure 2b; Figure S4, Supporting Information). Thus, we fabricated a CZZ-400 device, which contains a greater proportion of thicker ZnO phase compared to CZZ-300. The CZZ-400 device had the highest response at 100 °C (≈215) but showed significantly less reactivity at 150 °C (≈81) when contrasted with the response of CZZ-300 (≈1371). In the

case of the CZZ-500, the sensing channel exhibited metallic conductivity showing no response to the NO₂ exposure. We hypothesize that this difference in reactivity may be ascribed to the excessive growth of ZnO crystals in the CZZ-400 and 500 devices. This can be supported by the fact that the size of ZnO crystallites in the CZZ-400 and 500 was 7.8 and 21.8 nm, respectively, when the XRD patterns of ZnOs were analyzed with the Scherrer equation. To further validate this, we tested a 500-nm-thick pure ZnO film produced via e-beam deposition. The sensor showed a peak response of ≈4.5 and ≈2.8 at 250 and 150 °C, respectively, significantly lower than the CZZ devices, thereby corroborating our hypothesis. The annealing temperature-dependent reactivity can be inferred from the intrinsic conductivity of the materials as exhibited in the real-time conductivity measurements (Figure S10, Supporting Information). In all instances, the resistance of the ZIF-8 film decreased significantly ≈280 °C, reaching a plateau with a certain level. Specifically, the overall conductivity increased at higher annealing temperatures, suggesting an increase in oxide density. Of these, the 300 and 400 °C annealed samples demonstrated a range of resistivity close to semiconductors, favorable for a high gas sensing response.^[62] Therefore, the density of nanophasic ZnO formation seems to be a critical determinant of the sensing properties. Moreover, we created another CZZ-300 device, beginning with the drop-casting of powder-type ZIF-8 onto the bare sensor electrode (CZZ-300_P), to investigate the impact of the connectivity of the conducting channel on sensing performance.^[63] While the CZZ-300_P sensor displayed a fairly high response at 200 °C (≈91.5), its response was considerably lower (≈16.4) than that of the film-type CZZ-300 device at the temperature of 150 °C.

We conducted further evaluations of sensing properties by varying gas conditions at the optimal temperature. First, we performed gas concentration-dependent sensing experiments to evaluate its capacity for quantitative analysis (Figure 4c; Figure S11, Supporting Information). The desired gas concentration was prepared by diluting 10 ppm NO₂ gas with synthetic air with a specific ratio by using a mass flow controller (MFC). We composed 2, 4, 6, 8 10 ppm of the gas and exposed them to the device. The normalized resistance plot revealed that the electric signal amplitude was proportional to the gas concentration, and the response displayed a strong correlation with linear regression (Figure 4d). The minimum detection limit for NO₂ gas was determined to be 0.63 ppb, calculated using the fitting curve where the signal-to-noise ratio reaches 3 (3σ method).^[64]

We also investigated the effect of humidity on the sensing capabilities (Figure 4e,f; Figure S12, Supporting Information). To generate the desired humidity level, synthetic air (0% humidity) was passed through deionized water (18 MΩ) to achieve a water-saturated carrier gas. The bubbled gas was then mixed with synthetic air in desired ratios using MFCs. Then, the device was sequentially exposed to various humidity levels, ranging from 0% to 80% with 20% intervals, from the baseline stabilization step. Upon introducing humid air into the sensing chamber, the resistance of the sensor decreased due to the adsorption of H₂O molecules on the n-type ZnO (Figure S12, Supporting Information). We also mixed humid air with NO₂ gas for experimental consistency and exposed them to a sensor. The resultant responses for humid 2 ppm NO₂ were calculated as 341.2 (0% RH), 664.6 (20% RH), 698.0 (40% RH), 756.6 (60% RH), and 685.3

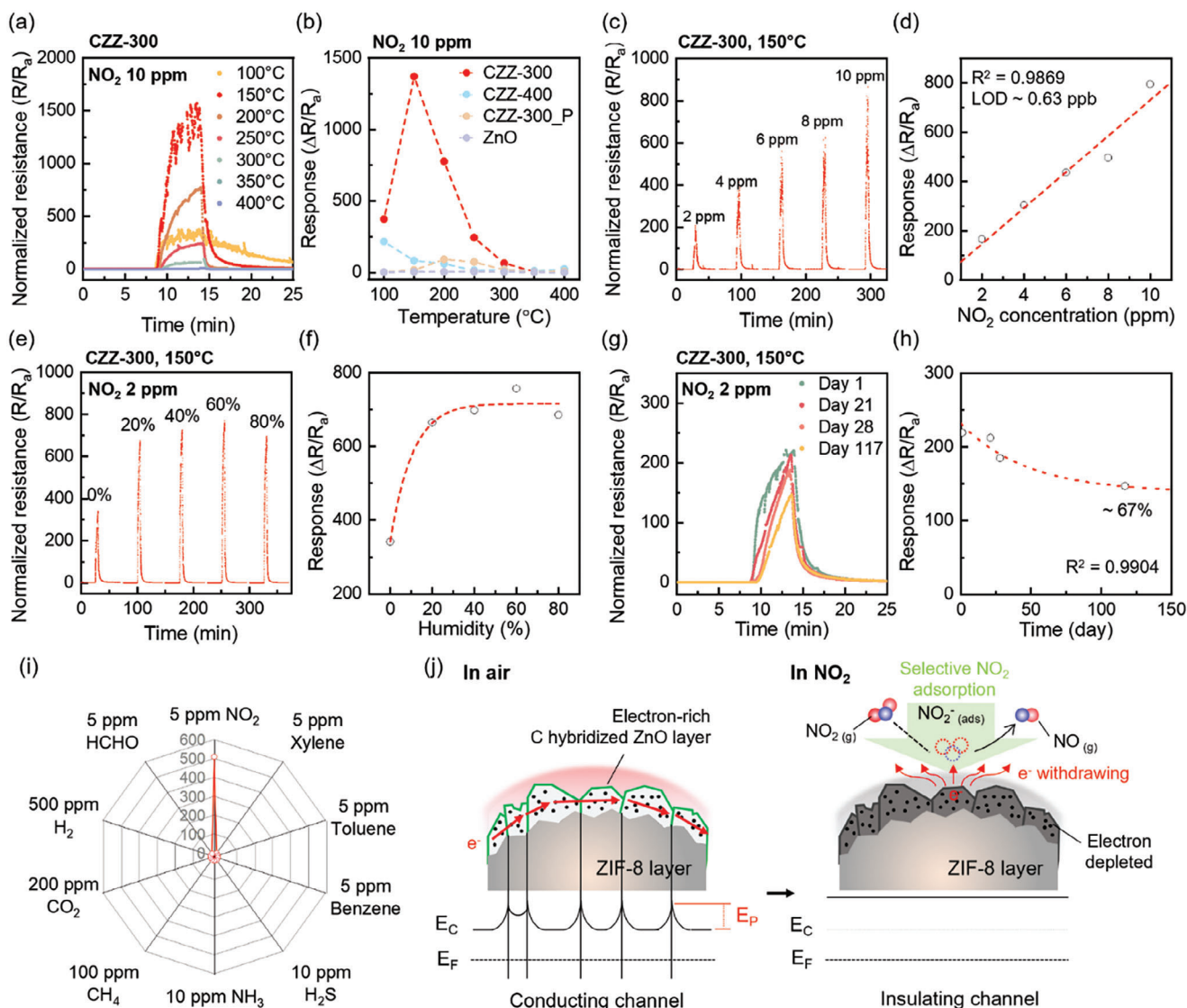


Figure 4. Gas response properties of N-carbon hybridized ZnO/ZIF-8 (CZZ). a) Normalized resistance curve obtained from a CZZ-300 sensor at various operating temperatures with 10 ppm NO₂ gas exposure. b) Temperature-dependent sensing responses of ZnO thin film, powder type CZZ-300 (CZZ-300_P), CZZ-300, and CZZ-400 sensors to 10 ppm NO₂ gas. c) Normalized resistance curve of a CZZ-300 gas sensor to NO₂ gas exposure of various concentrations (2, 4, 6, 8, and 10 ppm). d) Calculated sensor response obtained from each NO₂ concentration and linear fitting curve. e) Normalized resistance curve at various humidity conditions (0%, 20%, 40%, 60%, and 80%) with 2 ppm NO₂ gas exposure and f) calculated responses. g) Long-term stability of a CZZ-300 sensor tested up to 117 days and h) measured responses. i) Diagram depicting the selective response of CZZ-300 sensors to various gas compounds. j) Illustration of the NO₂-selective sensing mechanism of the CZZ-300 sensor.

(80% RH) (Figure 4e). Interestingly, we observed that the signal amplitude was approximately doubled in humid conditions compared to values measured in dry environments, indicating enhanced sensitivity in the presence of moisture. Moreover, according to our fitting curve (Figure 4f), the effect of high humidity level (>20%) appeared negligible, and small amounts of water (<20%) were enough to enhance response signals, possibly due to the nanoscale feature size of the sensing channel.

Next, we assessed the long-term stability of the device by storing it in ambient air conditions ($\approx 25^\circ\text{C}$) for 117 days (Figure 4g,h). During this time, the signal amplitude decreased to $\approx 67\%$ of its initial value, and the response time was degraded

from ≈ 180 s to ≈ 215 s. We observed a few fluctuations in the baseline resistance (Figure S13, Supporting Information) but confirmed that the CZZ-300 sensors still maintained excellent sensitivity. In terms of the reproducibility of sensing properties, we exposed NO₂ gas 5 times in a row and measured response (Figure S14, Supporting Information). Despite an upshift in the baseline resistance due to residual NO₂ molecules, the sensing performance remained stable without significant degradation.

To evaluate the potential applications of CZZ-300 sensors in environments containing mixed gases, we examined their detection selectivity by testing various gases (Figure 4i; Figure S15, Supporting Information). Since NO₂ is primarily produced

during the combustion of fossil fuels,^[65] we used representative abundant atmospheric gases (H_2 , CO_2 , and NH_3), hydrocarbon (CH_4), and volatile organic compounds (formaldehyde, benzene, toluene, and xylene) as potential interference gases. In addition, certain inflammatory diseases such as asthma, chronic obstructive pulmonary disease, and certain types of cancers could lead to elevated fractional exhaled nitric oxide (FE_{NO}), easily detected in the NO_2 level.^[66–68] Therefore, we further screened H_2S gas, one of the main components in exhaled breath. Individual gas was exposed to the CZZ-300 sensor once at a time at $150\text{ }^\circ\text{C}$ through the gas exposure system. The results demonstrated that most gases either displayed no response or a negligible one (<1) even when present in the same or much higher concentrations, indicating that the sensor has a significantly high selectivity toward NO_2 molecules. We further confirmed the reliable detection of NO_2 content by noting no substantial difference in response profile between single gas (2 ppm NO_2) and mixed gas (40 ppm CH_4 , 20 ppm CO_2 , and 2 ppm NO_2) environments (Figure S16, Supporting Information).

Our experimental results indicate superior NO_2 detection properties for the CZZ-300 device when compared to other sensing materials, including ZnO-based micro/nanostructures, conducting MOFs, and low-dimensional nanomaterials (Figure S17, Table S1, Supporting Information). The responses were normalized in terms of concentration (sensitivity, ppm^{-1}) due to the varying NO_2 concentrations used across different studies. Notably, the CZZ-300 device demonstrated exceptional sensitivity, even under humid conditions. When compared to metal oxide sensors, the CZZ-300 device also functioned at a relatively lower operating temperature ($150\text{ }^\circ\text{C}$), except for the UV light-requiring or hybridizing with nanomaterial cases.^[69,70] In terms of detection selectivity, despite most sensing materials displaying higher responsiveness to NO_2 gas, their selectivity is low and susceptible to false-positive results from high concentrations of interfering gases. Conversely, CZZ-300 exhibited almost exclusive selectivity to NO_2 compared to various atmospheric gases, hydrocarbons, and VOCs. While the response and recovery times of CZZ-300 were marginally slower than other sensing materials, its durability was confirmed through long-term stability and reproducible detection tests. Moreover, its scalable on-chip fabrication method ensures a high production yield, potentially enabling an easily exchangeable platform. Overall, CZZ-300 exhibits superior performance in terms of high sensitivity, selective NO_2 detection, functionality, and scalability.

We briefly expressed the possible detection mechanism for NO_2 gas in Figure 4j. According to our earlier characterization, CZZ-300 is composed of polycrystalline ZnO layers with a ZIF-8 core structure. In the air atmosphere, despite the existence of an energy potential barrier (E_p) that impedes the transport of electrons across zinc oxide (ZnO) grains, heat-excited electrons maintain free movement under operational temperature. Exposure of CZZ-300 to NO_2 gas induces the direct withdrawal of electrons from the conduction band of the ZnO phase by NO_2 molecules or a reaction with ionized oxygens adsorbed on the ZnO.^[71] This action initiates the formation of electron-depleted regions in the ZnO layer, resulting in a substantial elevation of the E_p and a significant rise in resistance level.

One of the distinguishable characteristics of CZZ-300 is the several nanometric dimensions of a ZnO layer. Usually, the am-

plitude of the sensing response is primarily governed by the alteration in the electron depletion layer relative to the sensing material dimensions. In other words, sensing materials with smaller dimensions, such as nanoparticles and quantum dots, tend to exhibit higher responses compared to bulk materials. In that point of view, CZZ-300 has only a few nanometers thick ZnO layer, analogous to the electron Debye length so that sensor sensitivity can reach a maximum.^[72] This finding is further substantiated by the observed decrease in response as ZIF-8 is subjected to higher temperatures (e.g., CZZ-400), leading to a thicker ZnO layer. Conversely, a CZZ-300 device produced under an inert nitrogen (N_2) atmosphere displayed negligible conductivity and remained unresponsive to NO_2 gas due to the lack of ZnO (Figure S18, Supporting Information), underlining the critical role of the ZnO layer on ZIF-8.

Hybridization of electron-rich N-carbon residues also can play a significant role in enhancing channel conductivity and detection sensitivity. These organic residues act as electron reservoirs, providing electrons to the oxide to achieve measurable conductivity even at a thickness of a few nanometers ($2.0 \times 10^{-4}\text{ S cm}^{-1}$ at $150\text{ }^\circ\text{C}$). Furthermore, the sensing reaction of NO_2 typically involves strong electron-withdrawing from the oxide. Injecting mobile charge carriers, for example, UV irradiation, can enhance NO_2 sensing capabilities, particularly at lower operating temperatures.^[73] In the same manner, these electron-enriched groups also serve as Lewis base sites that can highly interact with the strong Lewis acid molecule NO_2 through Lewis acid-base reactions. As a result, the sensitivity of the gas sensor is improved, making it more effective in detecting NO_2 gas with outstanding detection limits and lower operating temperatures.

The sensor demonstrates enhanced sensitivity under humid conditions, while many sensing materials are susceptible to impairment by humidity. Based on Figure S12 (Supporting Information), higher sensitivity in humid conditions can be mainly attributed to the decrease in baseline resistance of the sensing material in the presence of water. The decrement in baseline resistance is possibly due to the physisorption of H_2O molecules on the oxide, generating an impurity energy level in band energy structures and facilitating the excitation of electrons.^[74,75] While the water molecules can take the surface of the oxide layer, we expect that its binding energy is weak due to the relatively hydrophobic nature of organic dopants and the relatively high temperature of our sensing environment ($150\text{ }^\circ\text{C}$): water adsorption is an exothermic reaction. In addition, because NO_2 molecules have a higher affinity for the N-doped carbon ZnO due to the strong interaction between NO_2 and imidazole-derived organic compounds, the pre-adsorbed H_2O can be easily replaced by NO_2 .^[46,76] Therefore, the unique composition of the sensing layer could induce enhancement of sensing performances in humid conditions. However, we believe further study is necessary to understand the precise mechanism of H_2O adsorption on MOF-based chemiresistors, encompassing aspects such as adsorption sites, chemical bonding states, and binding energy. The sensor demonstrates enhanced sensitivity under humid conditions, while many sensing materials are susceptible to impairment by humidity.

Last, the superior selectivity of CZZ-300 can be ascribed to the competitive adsorption of NO_2 by the ZIF-8 structure. Gas adsorption measurements indicate that both CZZ-300 and

pristine ZIF-8 have a strong affinity for NO₂, significantly outpacing other gases (Figure S19, Supporting Information). This facilitates the competitive adsorption of NO₂ and contributes to the much longer dwell time of NO₂ molecules around the sensing channel, which guarantees efficient sensing reactions between ZnO and NO₂ molecules compared to other molecular species (Figure 4j).

3. Conclusion

We performed an in-depth investigation on the impact of surface oxidation on a ZIF-8 polycrystalline layer and the ensuing phase transition leading to the formation of conductivity. By implementing a straightforward thermal annealing process in an ambient environment, we enabled the emergence of a nanoscale polycrystalline ZnO layer on the ZIF-8 surface, which served as a conductive channel. The ZnO phase transformation was initiated at ≈300 °C and exhibited an enhanced crystallinity with increasing temperatures. Sequential exposure of the annealed ZIF-8 layer to a NO₂ atmosphere amplified the crystallinity of the oxide layer and generated interconnected conductive channels by eliminating carbon residues located in the interstitial sites of the ZnO crystals, a phenomenon associated with electron doping. The CZZ-300 device demonstrated exceptional sensitivity to NO₂ gas, which can be attributed to the matching dimensions of the ZnO phase with the electron Debye length. Moreover, the high and selective adsorption property of ZIF-8 toward NO₂ gas contributed to the exceptional detection selectivity of the device. Contrary to conventional oxide gas sensors, the CZZ-300 exhibited remarkable sensing performance in the presence of water vapor. Consequently, our CZZ-300 device is anticipated to find utility in a broad spectrum of NO₂ detection systems, including industrial settings, air pollution monitoring, and diagnostics for inflammatory diseases. Furthermore, the straightforward oxidation-induced MOF modification technique can be generalized to other types of MOF materials, paving the way for their application in a diverse range of gas-selective sensors, in addition to various electronic devices, catalysts, and energy-related applications.

4. Experimental Section

Fabrication of CZZ Devices: Interdigitated electrodes (20 μm wide patterns with a 5 μm gap) were fabricated on SiO₂/Si substrates (2000 Å) using conventional photolithography. This process involved patterning the electrodes and then depositing a 5 nm layer of Chromium (Cr) followed by a 100 nm layer of Gold (Au) metals through thermal deposition. After partially masking electrode pads for interconnection, a polycrystalline ZIF-8 monolayer was synthesized on the substrate using hydrothermal reactions. Additional details regarding the growth of ZIF-8 can be found in the extended Experimental Section of the supporting information. The ZIF-8 layer was then thermally annealed at specific temperatures (200, 300, 400, and 500 °C) for one hour with a ramping rate of 5 °C min⁻¹ inside a quartz tube. After the heat treatment, 10 ppm of NO₂ gas was flown into the quartz tube at a flow rate of 1000 sccm and a temperature of 150 °C for 5 min to etch thermally combusted organic residues, resulting in the formation of a conductive channel composed of N-doped carbon-hybridized ZnO/ZIF-8 nanoparticles.

Evaluation of Gas Sensing Performances: The gas exposure system is briefly illustrated in Figure S20 (Supporting Information). After fabricat-

ing CZZ devices, electrode pads were connected to a digital source meter/source measurement unit (SMU, Keithley 2450, Keithley Instruments) using Pt wire and silver paste. The electrical resistance of ZIF-8 layers or CZZ devices was measured under a compliance voltage of 10 V and recorded in real-time through customized LABVIEW software at a 1 Hz sampling rate. The working temperature of the devices was regulated automatically by a furnace that was controlled by the software. For all measurements, synthetic air (0% humidity) was utilized as the carrier gas. A certified gas cylinder containing 10 ppm of NO₂ gas (balanced with air) was used as the source of NO₂. The total gas flow rate was maintained at 1000 sccm throughout the experiment. To conduct quantitative detection of the gas, the 10 ppm NO₂ gas was diluted with synthetic air in a specific ratio using mass flow controllers. To consist of different humidity levels of the gases, water-saturated air was generated by bubbling deionized water (18 MΩ) and then diluted with synthetic air to achieve the desired humidity ratio. Before exposing target gases, the device was stabilized in synthetic air for at least 900 s. Then, the desired target gas was flown for 300 s. Finally, the device was recovered enough for at least 2400 s in the synthetic air.

Supporting Information

Supporting Information is available from the Wiley Online Library or from the author.

Acknowledgements

H.M. and O.K. contributed equally to this work. This work was supported by the Technology Innovation Program (No. 20013621, Center for Super Critical Material Industrial Technology) funded by the Ministry of Trade, Industry & Energy (MOTIE, Republic of Korea). The research was also supported by the Basic Science Research Program by the Ministry of Education (2019R1A6A1A11055660). This work was supported by the Strategic Networking & Development Program (RS-2023-00268523), Korea Initiative for fostering the University of Research and Innovation Program (2020M3H1A1077207), and National Core Materials Research Center (2022M3H4A3053304) funded by the Ministry of Science and ICT through the National Research Foundation of Korea. The authors would also like to thank Dr. Jonas Börgel (University of California, Berkeley) for the help in interpreting the NMR spectra and the chemical degradation pathway of MOFs.

Conflict of Interest

The authors declare no conflict of interest.

Data Availability Statement

The data that support the findings of this study are available from the corresponding author upon reasonable request.

Keywords

conductivity, gas sensing, metal oxides, metal–organic frameworks (MOFs), surface oxidation

Received: September 4, 2023

Revised: November 9, 2023

Published online:

[1] H. Furukawa, K. E. Cordova, M. O'keeffe, O. M. Yaghi, *Science* **2013**, *341*, 1230444.

- [2] J.-R. Li, R. J. Kuppler, H.-C. Zhou, *Chem. Soc. Rev.* **2009**, *38*, 1477.
- [3] J.-R. Li, J. Sculley, H.-C. Zhou, *Chem. Rev.* **2012**, *112*, 869.
- [4] Z. R. Herm, E. D. Bloch, J. R. Long, *Chem. Mater.* **2014**, *26*, 323.
- [5] K. Adil, Y. Belmabkhout, R. S. Pillai, A. Cadiau, P. M. Bhatt, A. H. Assen, G. Maurin, M. Eddaoudi, *Chem. Soc. Rev.* **2017**, *46*, 3402.
- [6] Q. Qian, P. A. Asinger, M. J. Lee, G. Han, K. Mizrahi Rodriguez, S. Lin, F. M. Benedetti, A. X. Wu, W. S. Chi, Z. P. Smith, *Chem. Rev.* **2020**, *120*, 8161.
- [7] J. A. Mason, M. Veenstra, J. R. Long, *Chem. Sci.* **2014**, *5*, 32.
- [8] M. P. Suh, H. J. Park, T. K. Prasad, D.-W. Lim, *Chem. Rev.* **2012**, *112*, 782.
- [9] K. Sumida, D. L. Rogow, J. A. Mason, T. M. McDonald, E. D. Bloch, Z. R. Herm, T.-H. Bae, J. R. Long, *Chem. Rev.* **2012**, *112*, 724.
- [10] L. Ma, C. Abney, W. Lin, *Chem. Soc. Rev.* **2009**, *38*, 1248.
- [11] J. Lee, O. K. Farha, J. Roberts, K. A. Scheidt, S. T. Nguyen, J. T. Hupp, *Chem. Soc. Rev.* **2009**, *38*, 1450.
- [12] A. Corma, H. García, F. X. Llabrés I Xamena, *Chem. Rev.* **2010**, *110*, 4606.
- [13] D. Yang, B. C. Gates, *ACS Catal.* **2019**, *9*, 1779.
- [14] S. Kumar, Y. Pramudya, K. Müller, A. Chandresh, S. Dehm, S. Heidrich, A. Fediai, D. Parmar, D. Perera, M. Rommel, L. Heinke, W. Wenzel, C. Wöll, R. Krupke, *Adv. Mater.* **2021**, *33*, 2103316.
- [15] N. A. Travlou, K. Singh, E. Rodríguez-Castellón, T. J. Bandoz, *J. Mater. Chem. A* **2015**, *3*, 11417.
- [16] T. Zhou, Y. Sang, X. Wang, C. Wu, D. Zeng, C. Xie, *Sens. Actuators, B* **2018**, *258*, 1099.
- [17] M.-S. Yao, W.-X. Tang, G.-E. Wang, B. Nath, G. Xu, *Adv. Mater.* **2016**, *28*, 5229.
- [18] H. Tian, H. Fan, M. Li, L. Ma, *ACS Sens.* **2016**, *1*, 243.
- [19] X. Tu, F. Gao, X. Ma, J. Zou, Y. Yu, M. Li, F. Qu, X. Huang, L. Lu, *J. Hazard. Mater.* **2020**, *396*, 122776.
- [20] W. Li, Y. Zhang, C. Zhang, Q. Meng, Z. Xu, P. Su, Q. Li, C. Shen, Z. Fan, L. Qin, G. Zhang, *Nat. Commun.* **2016**, *7*, 11315.
- [21] L. S. Xie, G. Skorupskii, M. Dinca, *Chem. Rev.* **2020**, *120*, 8536.
- [22] L. Sun, T. Miyakai, S. Seki, M. Dinca, *J. Am. Chem. Soc.* **2013**, *135*, 8185.
- [23] L. Sun, C. H. Hendon, M. A. Minier, A. Walsh, M. Dinca, *J. Am. Chem. Soc.* **2015**, *137*, 6164.
- [24] L. Sun, C. H. Hendon, S. S. Park, Y. Tulchinsky, R. Wan, F. Wang, A. Walsh, M. Dinca, *Chem. Sci.* **2017**, *8*, 4450.
- [25] M. G. Campbell, D. Sheberla, S. F. Liu, T. M. Swager, M. Dinca, *Angew. Chem., Int. Ed.* **2015**, *54*, 4349.
- [26] S. S. Shinde, C. H. Lee, J.-Y. Jung, N. K. Wagh, S.-H. Kim, D.-H. Kim, C. Lin, S. U. Lee, J.-H. Lee, *Energy Environ. Sci.* **2019**, *12*, 727.
- [27] D. Sheberla, L. Sun, M. A. Blood-Forsythe, S. Er, C. R. Wade, C. K. Brozek, A. Aspuru-Guzik, M. Dinca, *J. Am. Chem. Soc.* **2014**, *136*, 8859.
- [28] X. Huang, P. Sheng, Z. Tu, F. Zhang, J. Wang, H. Geng, Y. Zou, C.-A. Di, Y. Yi, Y. Sun, W. Xu, D. Zhu, *Nat. Commun.* **2015**, *6*, 7408.
- [29] J.-H. Dou, L. Sun, Y. Ge, W. Li, C. H. Hendon, J. Li, S. Gul, J. Yano, E. A. Stach, M. Dinca, *J. Am. Chem. Soc.* **2017**, *139*, 13608.
- [30] D. Chen, H. Xing, Z. Su, C. Wang, *Chem. Commun.* **2016**, *52*, 2019.
- [31] G. Haider, M. Usman, T.-P. Chen, P. Perumal, K.-L. Lu, Y.-F. Chen, *ACS Nano* **2016**, *10*, 8366.
- [32] L. Qu, H. Iguchi, S. Takaishi, F. Habib, C. F. Leong, D. M. D'alessandro, T. Yoshida, H. Abe, E. Nishibori, M. Yamashita, *J. Am. Chem. Soc.* **2019**, *141*, 6802.
- [33] X. Kuang, S. Chen, L. Meng, J. Chen, X. Wu, G. Zhang, G. Zhong, T. Hu, Y. Li, C.-Z. Lu, *Chem. Commun.* **2019**, *55*, 1643.
- [34] M. G. Campbell, S. F. Liu, T. M. Swager, M. Dinca, *J. Am. Chem. Soc.* **2015**, *137*, 13780.
- [35] M. L. Aubrey, M. T. Kapelewski, J. F. Melville, J. Oktawiec, D. Presti, L. Gagliardi, J. R. Long, *J. Am. Chem. Soc.* **2019**, *141*, 5005.
- [36] E. Choi, S. J. Hong, Y.-J. Kim, S. E. Choi, Y. Choi, J. H. Kim, J. Kang, O. Kwon, K. Eum, B. Han, D. W. Kim, *Adv. Funct. Mater.* **2021**, *31*, 2011146.
- [37] E. Choi, J. I. Choi, Y.-J. Kim, Y. J. Kim, K. Eum, Y. Choi, O. Kwon, M. Kim, W. Choi, H. Ji, S. S. Jang, D. W. Kim, *Angew. Chem., Int. Ed.* **2022**, *61*, e202214269.
- [38] G. Ren, Z. Li, W. Yang, M. Faheem, J. Xing, X. Zou, Q. Pan, G. Zhu, Y. Du, *Sens. Actuators, B* **2019**, *284*, 421.
- [39] M. Zhan, S. Hussain, T. S. Algarni, S. Shah, J. Liu, X. Zhang, A. Ahmad, M. S. Javed, G. Qiao, G. Liu, *Mater. Res. Bull.* **2021**, *136*, 111133.
- [40] D. Matatagui, A. Sainz-Vidal, I. Gràcia, E. Figueras, C. Cané, J. M. Saniger, *Sens. Actuators, B* **2018**, *274*, 601.
- [41] C. Wang, J. Kim, J. Tang, M. Kim, H. Lim, V. Malgras, J. You, Q. Xu, J. Li, Y. Yamauchi, *Chem* **2020**, *6*, 19.
- [42] J. Hao, D. J. Babu, Q. Liu, P. A. Schouwink, M. Asgari, W. L. Queen, K. V. Agrawal, *Chem. Mater.* **2021**, *33*, 4035.
- [43] J. B. James, Y. S. Lin, *J. Membr. Sci.* **2017**, *532*, 9.
- [44] X. Zhang, J. Qin, R. Hao, L. Wang, X. Shen, R. Yu, S. Limpanart, M. Ma, R. Liu, *J. Phys. Chem. C* **2015**, *119*, 20544.
- [45] Y. Ding, L. Niu, Y. Chen, M. Wang, *Cryst. Res. Technol.* **2023**, *58*, 2300015.
- [46] S. Bhattacharyya, R. Han, J. N. Joshi, G. Zhu, R. P. Lively, K. S. Walton, D. S. Sholl, S. Nair, *J. Phys. Chem. C* **2019**, *123*, 2336.
- [47] H.-T. Wang, Y.-P. Liu, H. Zhang, N. Chang, W. Shao, M.-S. Shi, D. Ao, M.-C. Lu, *Microporous Mesoporous Mater.* **2019**, *288*, 109548.
- [48] A. S. Alshammari, L. Chi, X. Chen, A. Bagabas, D. Kramer, A. Alromaeh, Z. Jiang, *RSC Adv.* **2015**, *5*, 27690.
- [49] J. F. Watts, J. Wolstenholme, *An introduction to surface analysis by XPS and AES*, Wiley, Hoboken, NJ **2019**.
- [50] W. He, R. Ibraimov, A. Raslin, I. Hod, *Adv. Funct. Mater.* **2018**, *28*, 1707244.
- [51] M. Ayiania, M. Smith, A. J. R. Hensley, L. Scudiero, J.-S. Mcewen, M. Garcia-Perez, *Carbon* **2020**, *162*, 528.
- [52] A. Ganguly, S. Sharma, P. Papakonstantinou, J. Hamilton, *J. Phys. Chem. C* **2011**, *115*, 17009.
- [53] F. Tian, A. M. Cerro, A. M. Mosier, H. K. Wayment-Steele, R. S. Shine, A. Park, E. R. Webster, L. E. Johnson, M. S. Johal, L. Benz, *J. Phys. Chem. C* **2014**, *118*, 14449.
- [54] Z. Wei, M. Zhao, Z. Yang, X. Duan, G. Jiang, G. Li, F. Zhang, Z. Hao, *Proc. Natl. Acad. Sci. U. S. A.* **2023**, *120*, e2217148120.
- [55] S. Li, M. Hong, *J. Am. Chem. Soc.* **2011**, *133*, 1534.
- [56] K. Bouchmella, S. G. Dutremez, B. Alonso, F. Mauri, C. Gervais, *Cryst. Growth Des.* **2008**, *8*, 3941.
- [57] S. Sneddon, J. Kahr, A. F. Orsi, D. J. Price, D. M. Dawson, P. A. Wright, S. E. Ashbrook, *Solid State Nucl. Magn. Reson.* **2017**, *87*, 54.
- [58] M. Baranac-Stojanovic, *Chem. Asian J.* **2018**, *13*, 877.
- [59] S. H. Pang, C. Han, D. S. Sholl, C. W. Jones, R. P. Lively, *Chem. Mater.* **2016**, *28*, 6960.
- [60] X. Wu, S. Xiong, Z. Mao, S. Hu, X. Long, *Chemistry* **2017**, *23*, 7969.
- [61] R. Kumar, O. Al-Dossary, G. Kumar, A. Umar, *Nanomicro. Lett* **2015**, *7*, 97.
- [62] C. Wang, L. Yin, L. Zhang, D. Xiang, R. Gao, *Sensors* **2010**, *10*, 2088.
- [63] G. F. Fine, L. M. Cavanagh, A. Afonja, R. Binions, *Sensors* **2010**, *10*, 5469.
- [64] A. Shrivastava, V. Gupta, *Chron. Young Sci.* **2011**, *2*, 21.
- [65] S. C. Anenberg, J. Miller, R. Minjares, L. Du, D. K. Henze, F. Lacey, C. S. Malley, L. Emberson, V. Franco, Z. Klimont, C. Heyes, *Nature* **2017**, *545*, 467.
- [66] J. Hunt, *J. Allergy Clin. Immunol.* **2002**, *110*, 28.
- [67] J. Travers, S. Marsh, S. Aldington, M. Williams, P. Shirtcliffe, A. Pritchard, M. Weatherall, R. Beasley, *Am. J. Respir. Crit. Care Med.* **2007**, *176*, 238.
- [68] M. W. Pijnenburg, *Thorax* **2005**, *60*, 215.

- [69] Y. Xia, L. Zhou, J. Yang, P. Du, L. Xu, J. Wang, *ACS Appl. Electron. Mater.* **2020**, *2*, 580.
- [70] Z. Chen, H. Guo, F. Zhang, X. Li, J. Yu, X. Chen, *Adv. Mater. Interfaces* **2021**, *8*, 2101511.
- [71] Y. Song, F. Chen, Y. Zhang, S. Zhang, F. Liu, P. Sun, X. Yan, G. Lu, *Sens. Actuators, B* **2019**, *287*, 191.
- [72] P. Karnati, S. Akbar, P. A. Morris, *Sens. Actuators, B* **2019**, *295*, 127.
- [73] Z. Ma, Z. Wang, L. Gao, *Front. Chem.* **2021**, *9*, 811074.
- [74] M. Jin, S. Yan, D. Chen, *Chem. Phys.* **2020**, *538*, 110915.
- [75] M. Nagao, *J. Phys. Chem.* **1971**, *75*, 3822.
- [76] J. B. James, Y. S. Lin, *J. Phys. Chem. C* **2016**, *120*, 14015.